Diffusive Spin Transport in Narrow Two-Dimensional-Electron-gas Channels

F. Eberle, D. Schuh, D. Bougeard, D. Weiss⬤, and M. Ciorga*

Institute for Experimental and Applied Physics, University of Regensburg, D-93040 Regensburg, Germany

Using the geometry of the spin field-effect transistor, we investigate the spin transport of in-plane spins in an array of narrow channels formed in a two-dimensional electron gas confined in an (In, Ga)As quantum well. We demonstrate a clear enhancement of the spin-diffusion length with decreasing channel width, yielding up to 10 μm for the narrowest channels. We discuss the observed enhancement in terms of the suppression of the Dyakonov-Perel mechanism of spin relaxation, which has been invoked in previous studies in the case of diffusion of out-of-plane oriented spins. We also show that the spin signal is significantly higher when injecting into an array of narrow channels, compared with injecting into a single narrow channel.

I. INTRODUCTION

Electron spins in a semiconductor structure are very promising candidates as controllable carriers of information in many novel spintronics devices [1,2]. A convenient way of manipulating spins in zinc-blende semiconductors is provided by the spin-orbit interaction (SOI) [3,4], well characterized by an effective k-dependent magnetic field about which the spins precess [5]. At the same time, however, the SOI is a main source of spin relaxation. In a diffusive system with SOI, each scattering event changes the direction and/or value of the internal effective field, randomizing spin polarization in a process known as the Dyakonov-Perel (DP) mechanism [6]. This limits the length over which the spin polarization can be transferred within a device, also reducing the spin-related signal at the point of detection. It is important then to find a balance between positive and negative aspects of the SOI in terms of spin manipulation and spin transport.

One of the ways of increasing spin relaxation times in two-dimensional-electron-gas (2DEG) systems is to confine the spin transport into a very narrow channel [7–13]. In a one-dimensional (1D) limit, when the width of the channel is comparable to the Fermi wavelength, backscattering from impurities reverses only the direction of the SOI field. Spin rotations are limited then to a single axis, which effectively suppresses the DP mechanism. It has been predicted, however, that such a suppression starts at a larger channel width, when it becomes comparable with the spin precession length [7,13], which in semiconductors can be of the order of single micrometers, often larger than the mean free path of the system. Subsequent investigations confirmed these predictions for out-of-plane

spins in experiments involving the diffusion of optically generated spin polarization and in weak antilocalization studies [9–12].

Here, we experimentally investigate the effect of channel narrowing on the transport of electrically injected in-plane spins in a lateral device, i.e., in a geometry typical for a spin field-effect transistor [14]. We electrically inject in-plane spins into the transport channel consisting of an array of narrow wires defined in a 2DEG confined in a 20-nm-wide GaAs/In$_{0.09}$Ga$_{0.91}$As/Al$_{0.33}$Ga$_{0.67}$As quantum well and subsequently detect them using the nonlocal spin-valve technique [15–17]. The injected spins diffuse towards the detector in the presence of the SOI, and as a result of diffusion they dephase, resulting in a decay of the spin signal on the scale given by the diffusion length $\lambda_s = \sqrt{D\tau_s}$, where D is the diffusivity and τ_s the spin relaxation time. We show that narrowing the transport channel enhances the spin relaxation time, which we register as an enhanced spin-diffusion length λ_s. The latter increases from 4 μm, as measured for the wide channels, to around 10 μm, as measured for the narrowest channels with a width of 400 nm. Additionally, we discuss how the geometry itself affects the generation and flow of the spin current in a lateral spin-valve device and why an array of narrow channels is more efficient than a single channel.

II. EXPERIMENTAL DETAILS

In Fig. 1 we show the schematic of the spin-injection devices used in our experiments. They are all defined as mesas oriented along the $x \parallel [010]$ crystallographic direction. The mesas are fabricated from a single semiconductor wafer grown by molecular beam epitaxy (MBE) on a (001) GaAs substrate, with the following layer sequence

---

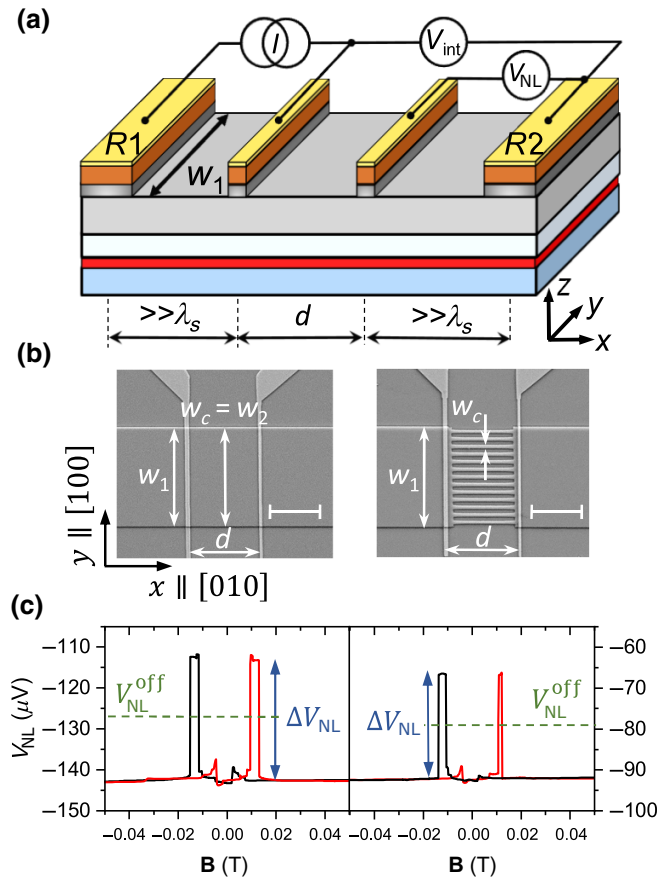*mariusz.ciorga@physik.uni-regensburg.de

FIG. 1. (a) Sketch of the lateral spin-injection device. Narrow ferromagnetic (Ga, Mn)As contacts on top of the channel, 500 nm and 700 nm wide, are used to inject/detect spin accumulation in the 2DEG. Additional contacts on both ends of the channel ($R1$, $R2$), far away from the spin aligning contacts, serve as a reference. (b) Scanning electron microscope pictures of two samples, representing two geometries used in the experiments. The scale bar corresponds to the length of 10 μm. Left panel: *standard* geometry with the width of the spin-transport channel w_c equal to the total width of the mesa w_1. Right panel: *array* geometry, with an array of N narrow wires, each of width w_c, in region 2 between injector and detector contacts. The total width of the 2DEG available for the spin transport is $w_2 = w_c = w_1$ for the standard geometry and $w_2 = N w_c$ for the array geometry. (c) Typical spin-valve signals measured for the standard geometry (left panel) and the array geometry with $N = 13$ and $w_c = 1$ μm (right panel). The red an black lines correspond to the magnetic field swept towards positive and negative values, respectively. The current used is $I = -20$ μA and distance between the contacts $d = 6$ μm. Horizontal dashed lines indicate the spin-independent offset voltage V_{NL}^{off}.

(in the order of growth): a 1000 nm GaAs/(Al, Ga)As superlattice, 95 nm of $Al_{0.33}Ga_{0.67}As$ with a Si δ-doping layer, a 20 nm $In_{0.09}Ga_{0.91}As$ layer, 100 nm of lightly Si-doped n-GaAs with 7×10^{16} cm^{-3}, a 15 nm $n^+ \rightarrow n$ transition layer followed by a 8 nm n^+ layer, where $n^+ \approx 5 \times$

10^{18} cm^{-3}, and a 2.2-nm-thick $Al_{0.33}Ga_{0.67}As$ layer. On top, a 50-nm-thick layer of ferromagnetic (Ga, Mn)As with an Mn content of 5.5% is grown, using low-temperature MBE. The (In, Ga)As layer forms a quantum well (QW), and a δ-doping layer placed within the (Al, Ga)As layer, 20 nm below the QW, allows the formation of a 2DEG in the QW. The top (Ga, Mn)As layer and the n^+-GaAs layer form a spin Esaki diode structure [18,19], which constitutes the highly efficient spin injecting and detecting system [16,17,20]. Electrical contacts are defined by optical or electron-beam lithography and subsequent evaporation of the Ti/Au metal system. The (Ga, Mn)As top layers are etched away in the region between the contacts to limit the lateral transport to the 2DEG. Before electrical experiments, the structure has to be illuminated to fill the electron states in the QW. Typical 2DEG parameters at a temperature of $T = 4.2$ K, after illumination, give the sheet resistance $R_s \approx 100$ Ω, the carrier density $n_s \approx 8.4 \times 10^{11}$ cm^{-2}, the mobility $\mu \approx 74\,000$ cm^2/V s and the mean free path $l_e \approx 1.1$ μm. These parameters change in the narrow wires, which is discussed further in Sec. III B.

Electrical spin injection takes place as a result of driving a charge current between the narrow *injector* contact placed close to the middle of the mesa and the reference contact on the left side of the mesa [Fig. 1(a)]. The orientation of the injected spins is determined by the magnetization orientation in the injector, which is kept along the [100] direction. The spin accumulation generated in the 2DEG underneath the injector diffuses in both directions along the channel: towards the reference contact on the left and towards the detector contact on the right. At the detector, the spin accumulation is detected as a nonlocal voltage V_{NL}, measured between the detector and the reference contact on the right side of the mesa. In our samples we typically use a 500-nm-wide contact as an injector, and a 700-nm-wide contact as a detector. We use two different geometries, displayed in Fig. 1(b), which differ in the way the region between the injector and detector, i.e., the actual spin-transport channel, is defined. In the following discussion, we refer to this region as region 2, whereas the region between each of the spin-aligning contacts and the corresponding reference contact we label as region 1. In the first geometry, which we further call the *standard* geometry, the widths of the regions 2 and 1 are equal, and given by the total width of the mesa w_1. The whole of region 2 constitutes in this case the spin-transport channel, with a width $w_c = w_2 = w_1$. In the second geometry, called the *array* geometry, region 2 consists of an array of N narrow wires, with the single wires of width w_c defining now the spin-transport channel relevant for the spin relaxation mechanism. The total width of the mesa available for spin transport in this case is then $w_2 = N w_c < w_1$. For all our array samples we use $w_1 = 20$ μm. To analyze the distance dependence of the spin signal, in case of the array

samples, four different devices with different injector-detector distances d are fabricated for each value of w_c. In case of the standard samples, for each value of w_c, we use a single device with four or five detector contacts.

III. RESULTS AND DISCUSSION

A. Spin accumulation profile

The spin accumulation at the detection point is probed by employing the spin-valve (SV) effect, i.e., switching of the nonlocal voltage as a result of rearranging the relative orientation of the magnetization in the injector and detector contacts between parallel and antiparallel directions [17,21]. An external magnetic field **B**, applied along the contact direction $y \parallel [100]$, is employed to switch between both configurations. A typical SV signal, as a result of sweeping **B** up and down, is shown in Fig. 1(c) for the standard geometry, with $w_c = w_1 = 20\ \mu$m, and the array geometry with $N = 13$ narrow wires and $w_c = 1\ \mu$m, respectively. The measured nonlocal voltage contains both a spin-dependent part V^s_{NL} and a spin-independent offset V^{off}_{NL}, typically observed in semiconductor spin valves [15,22,23]. The amplitude of the SV signal ΔV_{NL} is a measure of the spin accumulation and, from the distance dependence of ΔV_{NL}, one can extract spin-transport and spin-injection parameters.

Before we analyze the results of the experiments, let us discuss how the chosen geometry affects the generation and the transport of the spin accumulation and the corresponding nonlocal V_{NL}. The crucial parameter in describing geometrical effects is the spin resistance of the channel $R^*_{ch} = \rho\lambda_s^2/\upsilon = R_s\lambda_s/w$, where ρ is the resistivity of the channel, R_s its sheet resistance, λ_s the spin-diffusion

length, and $\upsilon = \lambda_s wt$ is the effective volume of the spin relaxation in the channel, with t being the thickness of the 2DEG layer and w the total width of the channel [24,25]. In the standard geometry [the left panel in Fig. 1(b)], the total channel width and the effective spin resistance are the same for regions 1 and 2. As a result, the injected spin current splits into two equal components, one going to the left and the other to the right of the injector, and the spin-related nonlocal voltage (assuming the tunneling regime) is given by [26]

$$V^s_{NL}(d) = \frac{\pm P^2 I R_s \lambda_s}{2w_c} \exp\left(-\frac{d}{\lambda_s}\right), \qquad (1)$$

where I is the injected current, P is the spin-injection efficiency, defined as the spin polarization of the injected current, and d the distance between the injector and the detector. Here, we assume that the spin-injection efficiency of the injector P_{inj} and of the detector contact P_{det}, are the same and equal to P, which generally holds for small currents [17]. The + (-) sign corresponds to the parallel (antiparallel) orientation of magnetizations in the injector and detector contacts. The spin-valve signal is then defined as $\Delta V_{NL} = 2V^s_{NL}$. The dependence of the spin-valve signal on the injector-detector separation length is therefore described by a simple exponential decay. In Fig. 2(a) we show the $\Delta V_{NL}(d)$ dependence for the standard sample with $w_c = 20\ \mu$m, which gives $\lambda_s \approx 4\ \mu$m.

In the array geometry [the right panel in Fig. 1(b)], the total width of the channel between the contacts $w_2 = Nw_c$ is smaller than the total width of the whole mesa w_1, i.e., $R^*_{ch,2} > R^*_{ch,1}$. The spin current injected into the 2DEG is therefore divided into two unequal components. One obtains in this case the following formula for $V_{NL}(d)$ [27]:

$$V^s_{NL}(d) = \pm\frac{2P^2 I R_{s,2}\lambda_2}{w_2}\frac{1}{[1 + (R_{s,2}\lambda_2 w_1/R_{s,1}\lambda_1 w_2)]^2 \exp(d/\lambda_2) + [1 - (R_{s,2}\lambda_2 w_1/R_{s,1}\lambda_1 w_2)]^2 \exp(-d/\lambda_2)}. \qquad (2)$$

The expression $R_{s,2}\lambda_2 w_1/R_{s,1}\lambda_1 w_2$ corresponds to the ratio of the effective spin resistances in regions 2 and 1, where $\lambda_{1(2)}$ and $R_{s,1(2)}$ indicate, respectively, the spin-diffusion length and sheet resistance in the corresponding regions, which are generally different. One can easily see that Eq. (2) becomes Eq. (1) for $\lambda_2 = \lambda_1 = \lambda_s$, $R_{s,2} = R_{s,1} = R_s$, and $w_2 = w_1 = w_c$. Although, in general, a simple exponential function does not describe the decay of the spin accumulation anymore, in some cases it can still be a good approximation. Namely, for $R_{s,2}\lambda_2 w_1/R_{s,1}\lambda_1 w_2 \gtrsim 1$ and $d/\lambda_2 \gtrsim 1$ the second exponential term in the denominator is negligible compared to the first one, resulting in the signal well described by

$$V_{NL}(d) \approx \frac{2P^2 I R_{s,2}\lambda_2}{w_2}\frac{1}{[1 + (R_{s,2}\lambda_2 w_1/R_{s,1}\lambda_1 w_2)]^2} \exp\left(-\frac{d}{\lambda_2}\right).$$

This holds for our samples, as demonstrated in Fig. 2(a) for the array sample with $N = 18$ and $w_c = 0.4\ \mu$m. From the slope of the plotted dependence, we extract $\lambda_s \approx 9.2\ \mu$m, which is substantially larger than for the case of a wide channel.

B. Spin relaxation and spin-diffusion length

The results of the measurements of the spin-diffusion length from the set of samples with different w_c and for different injection currents are plotted in Fig. 2(b). One can clearly observe that the narrowing of the transport

channel makes the transport of the in-plane spins more efficient. The spin-diffusion length remains constant at $\lambda_s^{2D} \approx$ 4 μm down to $w_c = 7.5$ μm, and then increases up to nearly 10 μm for the narrowest transport channel width of 400 nm. Before we analyze these results in relation to theoretical predictions and other experiments, let us briefly discuss the origin of the DP mechanism of spin relaxation.

The DP mechanism explains spin relaxation as a result of the precession of spins around the k-dependent effective magnetic field $\mathbf{B}_{\text{eff}}(\mathbf{k})$, resulting from the SOI [6,28], with the vector of the angular precession frequency defined as $\mathbf{\Omega}(\mathbf{k}) = (ge/2m)\mathbf{B}_{\text{eff}}(\mathbf{k})$, where g is the Landé g factor and m and e are the mass and the charge of an electron, respectively. In heterostructures based on zinc-blende semiconductors one distinguishes SOI contributions resulting from the structure inversion asymmetry (SIA), also called the Bychkov-Rashba contribution [29], and

(a)

(b)

FIG. 2. (a) Distance dependence of ΔV_{NL} for the standard sample with $w_c = 20$ μm and the wire sample with $w_c = 400$ nm for an injection current $I = -20$ μA. The values of the spin-diffusion length are obtained assuming exponential decay of the spin accumulation. (b) Spin-diffusion length versus the width of the transport channel w_c. The shown values are averages of values measured for currents of $I = -10, -20, -40$, and -100 μA [27]. Solid (open) symbols indicate the array (standard) geometry. The horizontal dashed line indicates the average spin-diffusion length obtained for wide channels, i.e., for the 2D case. The other dashed line shows the expected $\lambda_s(w_c) \propto w_c^{-1}$ dependence based on the diffusive theory. The solid blue line is just a guide for the eye. Inset: spin relaxation time $\tau_s(w_c) = \lambda_s^2/D$ calculated using D values determined from magnetotransport measurements.

bulk inversion asymmetry (BIA), called the Dresselhaus contribution [30]. Whereas the former depends linearly on $\mathbf{k}$, the latter has both linear and cubic components. The spin relaxation rate for spins oriented in the direction $i = x, y, z$ is in the motional narrowing regime given by the averaged square of $\mathbf{\Omega}(\mathbf{k})$ and is $\tau_{s,i}^{-1} = \tau_p(\overline{\Omega^2} - \overline{\Omega_i^2})$ [28]. For spins oriented in the [100] direction, this gives the following expression for the spin relaxation rate: $\tau_{s,y}^{-1} = (1/2)\tau_{s,z}^{-1} = (4Dm^*/\hbar^4)(\alpha^2 + \tilde{\beta}^2 + \beta_3^2)$, with $\tilde{\beta} = \beta_1 - \beta_3$, where α, β_1, β_3 are parameters describing Bychkov-Rashba, linear Dresselhaus, and cubic Dresselhaus contributions to the SOI, respectively [10,28]. In our experiments, we cannot distinguish between different SO mechanisms contributing to $\mathbf{B}_{\text{eff}}(\mathbf{k})$, but we can estimate the value of $\mathbf{B}_{\text{eff}}(\mathbf{k})$. Using the measured $\lambda_s^{2D} \approx 4$ μm and taking the diffusivity $D = (1/2)v_F l_e \approx 0.24$ m^2/s (where v_F is the Fermi velocity), we can estimate the spin relaxation time as $\tau_s^{2D} \approx 70$ ps, the total average effective spin-orbit field $B_{\text{eff}} \approx 2$ T, and $(\alpha^2 + \tilde{\beta}^2 + \beta_3^2)^{1/2} = (\tau_s^{2D}\hbar^4/4Dm^*)^{1/2} \approx 1.5 \times 10^{-13}$ eV m. As the cubic parameter β_3 depends on the sheet density, $\beta_3 = -\gamma(\pi n_s/2)$, where γ is a bulk Dresselhaus parameter, we can also evaluate it. Taking $\gamma \approx -10^{-29}$ eV m^3 [31] we get $\beta_3 = -\gamma(\pi n_s/2) \approx 1.3 \times 10^{-13}$ eV m [31]. This value suggests that the cubic contribution dominates the SOI in our samples. However, one has to take into account that the value of $(\alpha^2 + \tilde{\beta}^2 + \beta_3^2)^{1/2}$ is rather underestimated. In a more rigorous approach one should take into account the effectiveness of different momentum scattering mechanisms to the randomization of spins. This means that τ_p should be replaced by τ_p/a in the above formulas, typically with $a > 1$ [28].

In the first theoretical papers discussing the suppression of the DP mechanism in narrow channels, only the SIA contribution was considered [7,13]. In subsequent works also BIA and the cubic contribution were included [8,32,33]. It was shown that narrowing the channel suppressed both linear contributions, resulting in $\tau_s(w_c) \propto \tau_s^{2D}(w_c)^{-2}$. The cubic contribution, on the other hand, is not expected to be suppressed in diffusive wires. It typically slows down the overall suppression of the DP mechanism in such wires. In quantized 1D wires, however, the cubic contribution also becomes suppressed, decreasing with a decreasing number of available transverse modes [33]. These theoretical results have been confirmed in experiments involving optical studies of spin dynamics [10–12] as well as in transport experiments using weak antilocalization analysis [9]. All those experiments involved spins oriented perpendicular to the plane of the 2DEG. Whereas in some experiments a saturation of $\tau_s(w_c)$ for low w_c was observed and assigned to cubic BIA [10–12], in some of the experiments suppression of the cubic contribution was also discussed [9].
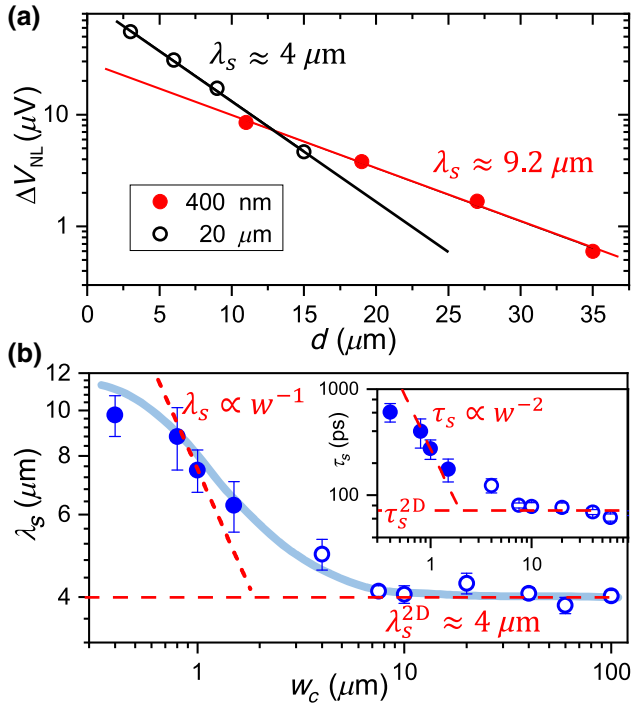
As we can see in Fig. 2, our results for in-plane spins are quite consistent with the predictions and observations discussed previously, as we obtain an enhanced $\lambda_s(w_c)$ compared to the 2D limit of approximately 4 μm, starting with $w_c \sim 4$ μm. It is clear, however, that λ_s increases more slowly than is predicted by the theory. One reason for that could be a decreasing momentum relaxation time upon decreasing w_c. Taking $D = (1/2)v_F^2\tau_p$ one gets $\lambda_s \propto \sqrt{\tau_p\tau_s}$, i.e., a decreasing $\tau_p(w_c)$ can slow down the enhancement of λ_s. It was reported, e.g., by Holleitner *et al.* [12], that for wires with $w_c < 2$ μm an increased boundary scattering leads to λ_s being limited by w_c, i.e., $\lambda_s \sim w_c$. This is clearly not the case for our samples as $\lambda_s > w_c$ for the narrow wires. Nevertheless, to take the effect of a decreasing τ_p into account, we carry out magnetotransport measurements on a different set of wire samples, fabricated from the same wafer as the spin devices [27]. Compared to the wide channels, we observe a clear reduction in mobility and thus also of τ_p and the mean free path in wires with $w_c \lesssim 1$ μm. For the 450-nm-wide wire the mobility and the mean free path are correspondingly 4800 cm^2/Vs and 0.76 μm, i.e., roughly 40% lower than for the wide channels. In the inset in Fig. 2(b) we plot $\tau_s(w_c) = \lambda_s^2/D$, calculated using the extracted values of the diffusion constant D. We find that τ_s in the narrowest wire is roughly an order of magnitude larger than in the 2D limit, although the rate of increase is slightly slower than the expected w_c^{-2} dependence. We would like to add that in all our samples we find w_c to be comparable to the electron mean free path l_e. Thus, we are in a crossover regime between diffusive and ballistic transport, different from the experiments in Refs. [11,12] but similar to those in Ref. [10].

C. Spin-injection efficiency

Our results clearly show that narrowing the channel increases the spin-diffusion length, leading to larger signals in the lateral spin-injection devices. We now discuss how the array geometry, in general, affects the magnitude of the measured spin signal for a given injector-detector separation d. In Fig. 3(a) we plot the measured spin-valve signal ΔV_{NL} versus the total channel width w_2 for an injecting current $I = -20$ μA and $d = 12$ μm for all samples. For comparison, we show the expected dependence based on Eqs. (1) and (2) for $P = 0.55$. In case of Eq. (2) we show both the case of $\lambda_2 = \lambda_1$, as well as $\lambda_2 = \lambda_2(w_c)$, as obtained from the measurements. For the standard geometry, the signal increases with decreasing $w_2 = w_c$, reflecting the $1/w_c$ dependence in Eq. (1). In the array geometry, on the other hand, decreasing w_2 leads to a decrease of the signal due to the increasing ratio w_1/w_2. This clearly demonstrates that for the array geometry with a given w_1 and w_c it is preferable to use a large number of wires, to keep $w_2 = Nw_c$ as close to w_1 as possible.
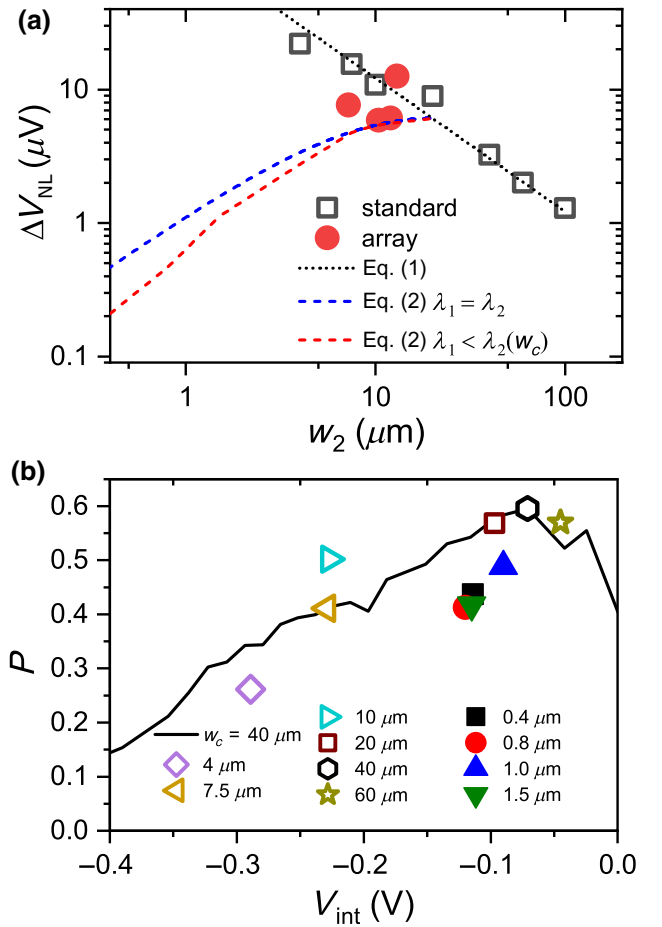

FIG. 3. (a) Dependence of the spin signal on the total width of the spin-transport channel w_2 for the standard and the wire samples, for the injector-detector separation $d = 12$ μm. The dashed curves are plotted using Eq. (1) (black) and Eq. (2), assuming constant $\lambda_2 = \lambda_1 = \lambda_s^{2D}$ (blue), and $\lambda_2 = \lambda_2(w_c)$ (red), as obtained from the measurements for $I = -20$ μA. For calculations we use a spin-injection efficiency of $P = 0.55$. In the case of Eq. (2) we use $w_1 = 20$ μm, as in experiments. (b) Spin-injection efficiency extracted from the measurements with the injection current $I = -20$ μA, as a function of the voltage drop across the interface V_{int}, for all measured samples (closed symbols, array geometry; open symbols, standard geometry). The solid line shows a typical drop of P with increasing V_{int}, as measured for the standard sample with $w_c = 40$ μm, with V_{int} adjusted by the injection current.

To explain why the array geometry is generally better than the standard geometry with a small w_c, we have to discuss the spin-injection efficiencies P obtained for both geometries. First, we would like to stress that for all discussed geometries our samples fulfill the condition for the tunneling regime of the spin injection, given by $R_{ch}^* \ll R_c^*$. Here, $R_c^* = R_c/(1 - P^2)$ is the effective spin resistance of the tunnel contact and $R_{ch}^* = R_s\lambda_s/w$ is the previously mentioned effective spin resistance of the channel. R_c is the electrical resistance of the contact, typically

amounting to ~ 7 $k\Omega$ for our 500 nm $\times 20$ μm injector contacts. For the standard samples with $w_c = 20$ μm, taking $R_s \approx 100$ Ω and $\lambda_s \approx 4$ μm we arrive at $R_{\mathrm{ch}}^* \approx 20$ Ω. For the array sample with $N = 18$, $w_c = 0.4$ μm, $R_s \approx 150$ Ω and $\lambda_s \approx 9$ μm we obtain $R_{\mathrm{ch}}^* \approx 190$ Ω. Taking $P \sim 0.5$, we get $R_c^* \approx 9.3$ $k\Omega$, i.e., the tunneling condition is clearly fulfilled for all our samples.

For standard samples, both R_c and R_{ch}^* scale as $1/w_1$. Therefore, simply narrowing the channel is not expected to change the injection condition, but it will affect P via a voltage drop across the interface at the spin-injecting contact V_{int}. In the tunneling regime, P is determined by the spin selectivity of the tunnel barrier. As reported before [17,20,34], in $(\mathrm{Ga},\mathrm{Mn})\mathrm{As}/\mathrm{GaAs}$ Esaki diode spin injectors, P typically decreases with increasing V_{int}. For a given injection current, V_{int} is inversely proportional to the contact area, i.e., also to w_1. As a result, it increases with decreasing width of the channel for standard samples, where $w_c = w_1$. Hence, using the array geometry allows one to decrease the width of the channel w_c, while keeping the size of the contact large enough to achieve low V_{int}, i.e., large P. This can be seen in Fig. 3(b), where we plot P vs V_{int}, extracted from the measurements on all samples, with the injection current $I = -20$ μA and, for comparison, from the measurements on the standard sample $w_c = 40$ μm for various injection currents. Since for all array samples we have $w_1 = 20$ μm, the corresponding V_{int} is approximately the same as for the standard sample with $w_c = 20$ μm. Although P is slightly lower for the array geometry, it is still larger than for the standard sample with $w_c = 4$ μm. In the previous discussion we neglect the Sharvin contact resistance [35,36] as we find it to be too small, compared with R_c^*, to affect the spin injection in our samples [27]. It is also worth noting, that the narrow standard mesas lead also to smaller aspect ratios of magnetic contacts. This negatively affects the magnetic switching, leading to poorly defined spin-valve patterns.

IV. SUMMARY

To summarize, we demonstrate a significant enhancement of the spin-diffusion length by narrowing the spin-transport channel in lateral, all-electrical spin-injection devices. This approach enables spin transfer over long distances, up to 10 μm in our narrowest channels. We find this enhancement of the diffusion lengths of the in-plane oriented spins to be consistent with theoretical and experimental work that describe diffusion of the out-of-plane oriented spins in narrow channels. We furthermore demonstrate that implementing an array of narrow channels instead of using a single channel exploits the advantages of our approach in the best possible way, allowing conservation of high spin-injection efficiencies, despite the channel narrowing. This can be important for design considerations of efficient spin field-effect transistorlike devices.

[1] J. Fabian, A. Matos-Abiague, C. Ertler, P. Stano, and I. Žutic, Semiconductor spintronics, Acta Phys. Slovaca **57,** 565 (2007).

[2] A. Hirohata, K. Yamada, Y. Nakatani, L. Prejbeanu, B. Diény, P. Pirro, and B. Hillebrands, Review on spintronics: Principles and device applications, J. Magn. Magn. Mater. **509,** 166711 (2020).

[3] R. Winkler, *Spin Orbit Coupling Effects in Two-Dimensional Electron and Hole Systems (Springer Tracts in Modern Physics)* (Springer, Berlin, 2003).

[4] J. Nitta, T. Akazaki, H. Takayanagi, and T. Enoki, Gate Control of Spin-Orbit Interaction in an Inverted $\mathrm{In}_{0.53}\mathrm{Ga}_{0.47}\mathrm{As}/\mathrm{In}_{0.52}\mathrm{Al}_{0.48}\mathrm{As}$ Heterostructure, Phys. Rev. Lett. **78,** 1335 (1997).

[5] R. Winkler, Spin orientation and spin precession in inversion-asymmetric quasi-two-dimensional electron systems, Phys. Rev. B **69,** 045317 (2004).

[6] M. I. D'yakonov and V. Y. Kachorovskii, Spin relaxation of Two-dimensional electrons in noncentrosymmetric semiconductors, Sov. Phys. Semicond. **20,** 110 (1986).

[7] A. A. Kiselev and K. W. Kim, Progressive suppression of spin relaxation in 2D channels of finite width, Phys. Rev. B **61,** 13115 (2000).

[8] S. Kettemann, Dimensional Control of Antilocalization and Spin Relaxation in Quantum Wires, Phys. Rev. Lett. **98,** 176808 (2007).

[9] Y. Kunihashi, M. Kohda, and J. Nitta, Enhancement of Spin Lifetime in Gate-Fitted InGaAs Narrow Wires, Phys. Rev. Lett. **102,** 226601 (2009).

[10] P. Altmann, M. Kohda, C. Reichl, W. Wegscheider, and G. Salis, Transition of a 2D spin mode to a helical state by lateral confinement, Phys. Rev. B **92,** 235304 (2015).

[11] A. W. Holleitner, V. Sih, R. C. Myers, A. C. Gossard, and D. D. Awschalom, Dimensionally constrained D'yakonov-Perel' spin relaxation in n-InGaAs channels: Transition from 2D to 1D, New J. Phys. **9,** 342 (2007).

[12] A. W. Holleitner, V. Sih, R. C. Myers, A. C. Gossard, and D. D. Awschalom, Suppression of Spin Relaxation in Submicron InGaAs Wires, Phys. Rev. Lett. **97,** 036805 (2006).

[13] A. G. Mal'shukov and K. A. Chao, Waveguide diffusion modes and slowdown of D'yakonov-Perel' spin relaxation in narrow 2-D semiconductor channels, Phys. Rev. B **61,** 2413 (1999).

[14] S. Datta and B. Das, Electronic analog of the electro-optic modulator, Appl. Phys. Lett. **56,** 665 (1990).

[15] X. Lou, C. Adelmann, S. A. Crooker, E. S. Garlid, J. Zhang, K. S. M. Reddy, S. D. Flexner, C. J. Palmstrøm, and P. A. Crowell, Electrical detection of spin transport in lateral ferromagnet–semiconductor devices, Nat. Phys. **3,** 197 (2007).

[16] M. Oltscher, M. Ciorga, M. Utz, D. Schuh, D. Bougeard, and D. Weiss, Electrical Spin Injection Into High Mobility 2D Systems, Phys. Rev. Lett. **113,** 236602 (2014).

[17] M. Ciorga, A. Einwanger, U. Wurstbauer, D. Schuh, W. Wegscheider, and D. Weiss, Electrical spin injection and detection in lateral all-semiconductor devices, Phys. Rev. B **79,** 165321 (2009).

[18] M. Kohda, Y. Ohno, K. Takamura, F. Matsukura, and H. Ohno, A spin Esaki diode, Jpn. J. Appl. Phys. **40,** 1274 (2001).

[19] E. Johnston-Halperin, D. Lofgreen, R. K. Kawakami, D. K. Young, L. Coldren, A. C. Gossard, and D. D. Awschalom, Spin-polarized zener tunneling in (Ga, Mn)As, Phys. Rev. B **65,** 041306 (2002).

[20] P. Van Dorpe, Z. Liu, W. Van Roy, V. F. Motsnyi, M. Sawicki, G. Borghs, and J. De Boeck, Very high spin polarization in GaAs by injection from a (Ga, Mn)As zener diode, Appl. Phys. Lett. **84,** 3495 (2004).

[21] M. Oltscher, F. Eberle, T. Kuczmik, A. Bayer, D. Schuh, D. Bougeard, M. Ciorga, and D. Weiss, Gate-tunable large magnetoresistance in an all-semiconductor spin valve device, Nat. Commun. **8,** 1807 (2017).

[22] F. L. Bakker, A. Slachter, J. P. Adam, and B. J. Van Wees, Interplay of Peltier and Seebeck Effects in Nanoscale Nonlocal Spin Valves, Phys. Rev. Lett. **105,** 136601 (2010).

[23] M. Johnson and R. H. Silsbee, Calculation of nonlocal baseline resistance in a quasi-one-dimensional wire, Phys. Rev. B: Condens. Matter Mater. Phys. **76,** 153107 (2007).

[24] A. Fert and H. Jaffrès, Conditions for efficient spin injection from a ferromagnetic metal into a semiconductor, Phys. Rev. B **64,** 184420 (2001).

[25] H. Jaffrès, J. M. George, and A. Fert, Spin transport in multiterminal devices: Large spin signals in devices with confined geometry, Phys. Rev. B **82,** 140408 (2010).

[26] J. Fabian and I. Zutic, *The Standard Model of Spin Injection, in Spintronics- From GMR to Quantum Information* (Forschungszentrum Juelich, Juelich, 2009), p. C1.

[27] See Supplemental Material at http://link.aps.org/supplemental/10.1103/PhysRevApplied.16.014010 for derivation of Eq. (2) and for the additional experimental data.

[28] I. Žutić, J. Fabian, and S. Das Sarma, Spintronics: Fundamentals and applications, Rev. Mod. Phys. **76,** 323 (2004).

[29] Y. A. Bychkov and E. I. Rashba, Oscillatory effects and the magnetic susceptibility of carriers in inversion layers, J. Phys. C **17,** 6039 (1984).

[30] G. Dresselhaus, Spin-orbit coupling effects in zinc blende structures, Phys. Rev. B **100,** 580 (1995).

[31] M. Kohda and G. Salis, Physics and application of persistent spin helix state in semiconductor heterostructures, Semicond. Sci. Technol. **32,** 073002 (2017).

[32] P. Wenk and S. Kettemann, Dimensional dependence of weak localization corrections and spin relaxation in quantum wires with rashba spin-orbit coupling, Phys. Rev. B **81,** 125309 (2010).

[33] P. Wenk and S. Kettemann, Direction dependence of spin relaxation in confined two-dimensional systems, Phys. Rev. B **83,** 115301 (2011).

[34] P. Van Dorpe, W. Van Roy, J. De Boeck, G. Borghs, P. Sankowski, P. Kacman, J. Majewski, and T. Dietl, Voltage-controlled spin injection in a (Ga,Mn)As/(Al,Ga)As zener diode, Phys. Rev. B **72,** 205322 (2005).

[35] A. Fert, J.-M. George, H. Jaffres, and R. Mattana, Semiconductors between spin-polarized sources and drains, IEEE Trans. Electron Devices **54,** 921 (2007).

[36] V. Kravchenko and E. Rashba, Spin injection into a ballistic semiconductor microstructure, Phys. Rev. B **67,** 121310 (2003).